Design, additive manufacturing, and characterisation of a three-dimensional cross-based fractal structure for shock absorption

Original
Design, additive manufacturing, and characterisation of a three-dimensional cross-based fractal structure for shock absorption / Viccica, Marco; Galati, Manuela; Calignano, Flaviana; Iuliano, Luca. - In: THIN-WALLED STRUCTURES. - ISSN 0263-8231. - ELETTRONICO. - 181:(2022). [10.1016/j.tws.2022.110106]

Publisher:
Elsevier

Published
DOI:10.1016/j.tws.2022.110106

Design, additive manufacturing, and characterisation of a three-dimensional cross-based fractal structure for shock absorption

Marco Viccica[a]*, Manuela Galati[a], Flaviana Calignano[a] and Luca Iuliano[a]

[a]*Integrated Additive Manufacturing Center (IAM) Politecnico di Torino, Department of Management and Production Engineering (DIGEP), Torino, Italy;*

luca.iuliano@polito.it

*Correspondence: marco.viccica@polito.it; Tel.: +39 0110907280

Fractal geometries have the potential to enhance the mechanical performances of materials. However, these geometries are often unfeasible using traditional processes. Focusing on selective laser sintering (SLS), an additive manufacturing process, this study investigates the mechanical properties of a 3D Greek Cross fractal. The mechanical behaviour of the structure is numerically investigated under quasi-static and dynamic compressive loads in the case of shock-absorbing head protection equipment applications. The material model is tailored and validated by experimental results. The energy absorption results higher up to 77% than traditional foam. However, for features smaller than 1 mm, the induced process defects drastically reduce the mechanical performance of the structure.

Keywords: 3D Greek cross fractal; personal protective equipment; selective laser sintering; 3D printing; PA12.

1 Introduction

Chaos is commonly called turbulence, undesirable randomness. However, over the past two decades, scientists have demonstrated that a chaotic system can develop in a fluid and orderly manner. There is a specific moment with a corresponding behaviour that is neither chaotic nor not chaotic, and there the transition to chaos occurs. Analysis of this transition has led to recognising phenomena that can frequently be described as fractal mathematics [1]. The term fractal was initially used by the mathematician Benoit Mandelbrot in 1975 [2] to represent a family of objects with specific characteristics, such as the same main form on all magnifying scales (self-similarity) and shape geometry, usually irregular and chaotic [3]. Fractals in nature are everywhere. Notable examples can be found in coastlines, flowers, trees, and animal shells [1–6].

Since Mandelbrot [2] formalised the fractal theory, numerous applications have been investigated in several fields such as physics [7,8], artistic objects (aesthetic use) [9], computer graphics [10–12], data security [13], mechanical transmission diagnosis [14,15], surface roughness [16,17]. Most of these literature works focused on the mathematical concept of fractal dimension. The interest in using fractal geometry to explore mechanical and thermal performance improvements has largely grown over the last decade. For instance, the interlocking properties of hierarchical fractal structures provided a better load distribution and energy absorption [18–21]. Farina et al. [18] analysed the bending behaviour of cement matrix composites reinforced by straight, fractal-shaped titanium alloy rods. The interlocking mechanisms between the fractal rods and the matrix increased the first crack strength by 152% with respect to the unreinforced counterpart. Similar mechanical properties can be provided by suture joint structures that are composites that join two interdigitate rigid components, called teeth, and a thin conforming layer distributed along a seam line [20–24]. Li et al. [20] showed how fractal-type patterns characterise the seam line of certain structures in biological systems. An increase in the hierarchy of fractal patterns, which corresponds to a higher order of teeth, can result in better tensile and shear load resistance capabilities. Another example of fractal structure application is the optimisation of fluid distribution through tree-like channels [25–28]. Wang et al. [25] showed that a fractal branching geometry applied to the heat exchanger channels could increase the heat transmission coefficient and reduce the pressure drop compared to a conventional heat exchanger. More in-depth studies of the tree-like fractal geometry effects were carried out for impact strength applications [29,30]. The energy absorption capability of thin-walled tubes with bio-inspired tree-like pattern cross-sections was investigated by San Ha Ngoc et al. [30]. It was proved that the branching structures were characterised by an optimal regular folding deformation of the thin wall in high hierarchical order. From a structural point of view, the results indicated better axial load stability than the corresponding single wall structure. Other projects have led to the development of thin-walled tube protective devices with innovative cross-sections based on fractal structures such as fractal-like honeycomb [31–34], Koch curve [35], side-fractal shape [36,37], and Sierpinski shape [38].

Despite these proved properties, the applications are today limited because these kinds of structures, especially three-dimensional geometries, are difficult to produce or often unfeasible by traditional manufacturing technologies. The production of relatively simple two-dimensional fractal structures with a constant cross-section was achieved using non-conventional manufacturing techniques such as the wire electric discharge machine (WEDM) [30,32,35,37].

Over the last few decades, the development of additive manufacturing (AM) processes has opened up several design opportunities, providing more freedom for fabricating such complex structures [39,40]. Nevertheless, the literature is still lacking, and only a few studies investigated the adoption of AM processes but are limited to 2D fractal geometries [18,21,28,41–45].

The present study applies an AM process for developing a 3D Greek cross fractal [46–51] for a novel application in head protection equipment. The mechanical properties are investigated considering polyamide 12 (PA12) produced by selective laser sintering (SLS). Quasi-static compression tests are numerically simulated by a finite element (FE) model and validated experimentally. The mechanical performance of the structure is also analysed by considering the variation of the diameter of the initiator object and the presence of multiple cells arranged in a 3D space. A methodology for numerically accounting for the peculiarity of the material produced by SLS is presented. Finally, the results of a simulated impact test are compared with data extracted from the literature for more traditional material.

The reason for this investigation is the result of the growing interest in the use of polymer-based AM technologies [52] for the production of high-performance helmets for sports [53–58], military [59,60]) and other biomedical applications [52]. The main requirements for these devices are high shock absorption levels and lightweight. For enhancing these properties, thin structures generated by bio-inspired shapes [61,62], lattice geometries [57,63,64], and topology optimised [62] parts are currently used. Fractal structures have never been explored, but according to the current literature, three-dimensional fractal geometries could represent a perfect candidate for crash motorcycle helmet liners.

2 Materials and Methods

2.1 Greek cross-based fractal design

Fractal geometry is the result of subsequent transformations of a simple geometrical object (line, triangle, square) defined as the “initiator” [2]. Based on deterministic or stochastic rules, these transformations generally follow recursive formulas in the domain of real or complex numbers. The simplest fractal construction method is based on affine transformations such as scaling, translation, rotation, reflection, and a combination of them [1].

The fractal structure used in this study is inspired by the mathematical 3D Greek cross presented by Dickau R. [47]. The initiator consists of a cross of three struts linearly extruded along the axes of a cartesian tern (Fig. 1). Each strut has a circular cross-section of diameter D that is constant at each n^{th}-step. At step n=1, the initiator consists of three struts whose length is equal to L_1^{st}. These struts cross at the origin point of the cartesian tern by generating six branches of size equal to $L_1^{st}/2$. At n^{th}-step, each branch of length $L_n^{th}{}_{-1}/2$ is assumed to be one of the three struts along principal axes; therefore, two struts of length $L_n^{th}{}_{-1}/2$ are added along the remained axes; these construction rules make the number of branches equal to 6^n at step n^{th}.

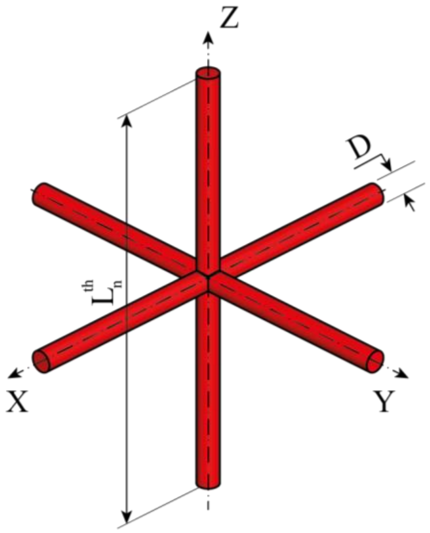

Fig. 1. 3D Greek cross initiator: D represents the size of the strut diameter; L_n^{th} is the strut length at the step n^{th}.

The transformation series of the structure stops within two iterations at the 3rd step. Additionally, it can be mathematically demonstrated that the final generated structure tends to be an octahedron for the n^{th}-step tending to infinity. The iteration steps used to generate the 3D cross-based fractal structure (3D-CFS) are highlighted, with different colours, in Fig. 2.

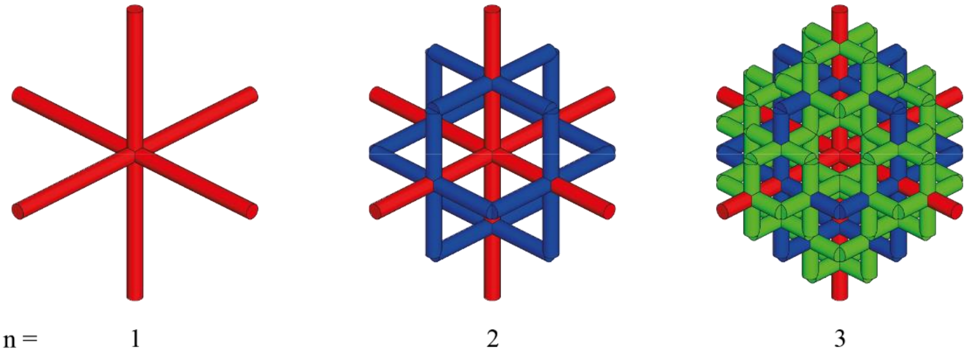

Fig. 2. 3D-CFS iterations: in red, the first step; in blue, the added axes of the second step; in green, the added axes of the third step.

The 3D-CFS design is parametric, and its global size depends on the two critical parameters mentioned above, L_n^{th} and D. Therefore, its size can be adjusted according to the production system, the material, and the final application of the structure. The first configuration proposed for the preliminary experimental tests consisted of a 3D-CFS developed in a cubic envelope of 40 mm side and 2 mm long diameter struts. Over successive iterations, the derived branches overlap at each extremity due to the 1/2 strut length scale factor. This overlapping generates sharp edges in which stress concentration may occur when the structure is under load. Also, when joining several cells, these extremities require geometrical adjustments, e.g., adding chamfers, as shown in Fig. 3.

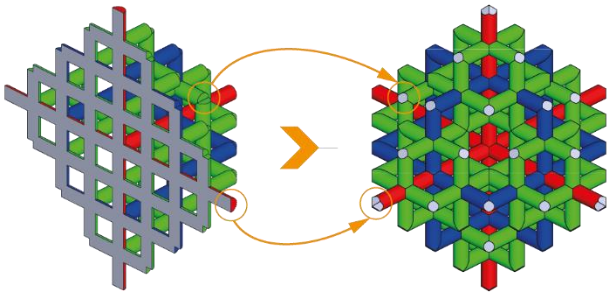

Fig. 3. Adjusting the sharp edges by applying chamfers, highlighted in the orange circles.

Using this construction, a cubic test sample was developed to assess the mechanical properties of the 3D-CFS by simulating a single repetitive cell of a multi-structure system. First, a single 3D-CFS was linearly replicated in the space (Fig. 4a); each structure is linked to the other by the extremities adequately modified on the struts (see Fig.3) generated at the first iteration. The connection is shown in Fig. 4b as the lateral section. Then, a region of interest corresponding to a cube of 40 mm side was extracted. Two square bases of 42 mm side and 2 mm thick have been added as continuous interfaces with the structure (Fig. 4c). These plates were used to apply the quasi-static compressive (or dynamic) load. An example of the structure is provided in STL format as supplementary material.

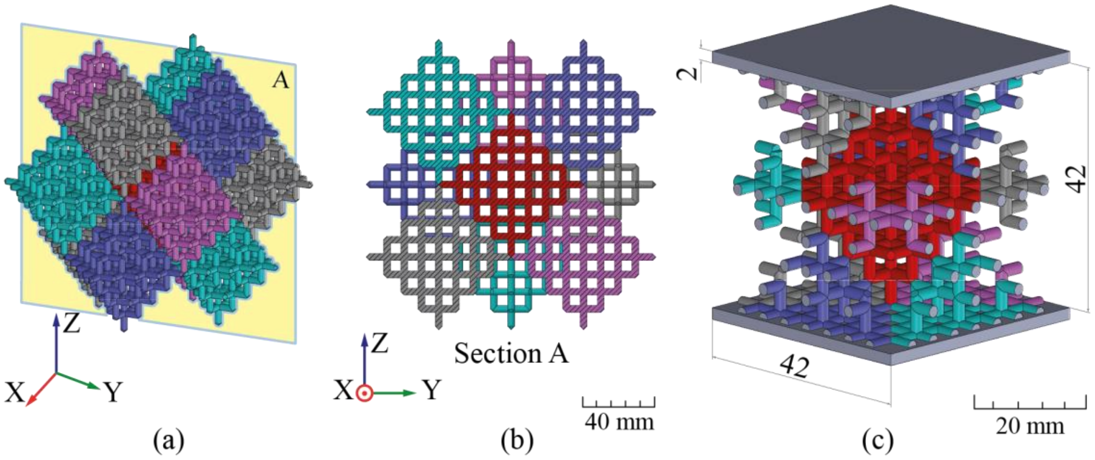

Fig. 4. (a) Space replication of the 3D-CFS and (b) its lateral section; (c) cubic sample after cuts. The portion of the structure in red highlights the main 3D-CFS of the cubic compression sample.

2.1.1 Diameter effect

A sensitivity analysis was carried out to study the effect of the cross-section strut dimension on the mechanical properties under compression loads. The diameter size of the struts was selected in the range from 1 mm to 2.5 mm by considering the mechanical and manufacturing constraints of the SLS process. Thinner features of the structure, i.e.

the struts with diameters of less than 0.5 mm, could be unfeasible because of the laser spot size. Also, small diameters lower the volume fraction (VF) of 3D-CFS structures that, under load, show lower stiffness and larger deformation with the rapid development of fractures. In contrast, larger diameters increase the volume fraction values, challenging the removal of unsintered powder trapped inside the structure. Moreover, denser structures increase the structure stiffness, leading to rapid densification with a limited plateau region of the stress-strain curve and, therefore, lower energy absorption. The diameter varied from 1 mm to 2.5 mm with a step of 0.5 mm. Each structure was identified by the structure diameter size and therefore as D1, D1.5, D2, and D2.5, respectively, (Fig. 5). Considering the octahedral envelope of the 3D-CFS as a solid material, the resulting volume fraction from the smallest to the largest diameter was 7.3%, 15.6%, 26.4% and 39.2%, respectively.

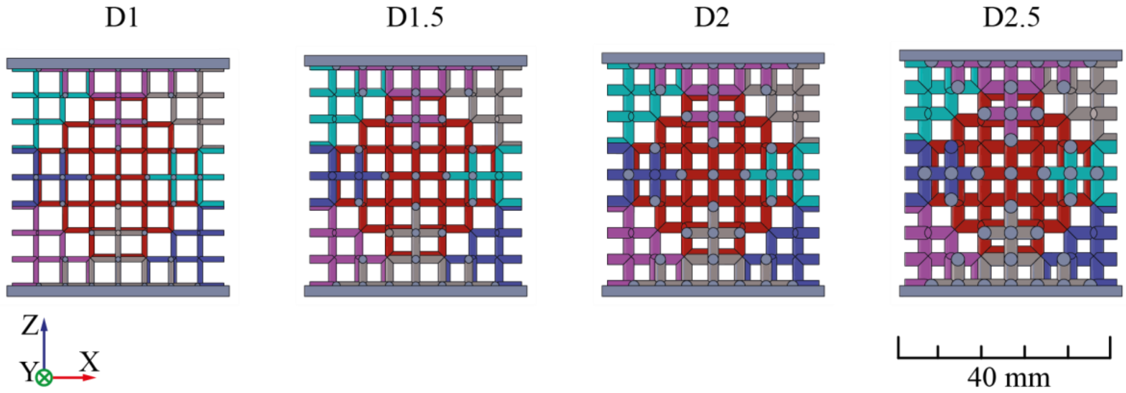

Fig. 5. Diameter variation of the 3D-CFS: from left to right, the size of the diameter varied from 1 mm to 2.5 mm.

2.1.2 *Multi-cell and scale effect*

The effect of the multi-cell on the compressive mechanical behaviour of the 3D-CFS cell was evaluated to emulate the application of the structure into a head impact protection device; specifically, the thickness of a motorcycle helmet was considered. Therefore, the structure was modified, assuming different adjustments to fit the chosen helmet better. Four configurations were designed and analysed numerically (Fig. 6). The cell named D2 was considered as the basis for obtaining different configurations without changing the volume fraction. The configuration named D2_50% (Fig. 6a) consisted of the nominal cell D2 scaled by a factor equal to 0.5. Therefore, the resulting diameter is 1 mm as the D1 structure, but the volume fraction is higher than the D1 counterpart. The configuration named D2_50%_2z was designed considering a stacking of two D2_50% cells along the Z-axis, which is the printing direction (Fig. 6b). The configurations D2_2×2 and D2_3×3 consist of a repetition of the cell D2 in the plane XY according to a square matrix 2×2 (Fig. 6c) and 3×3 (Fig. 6d). A resume of the geometrical feature of the described configurations is presented in Table 1.

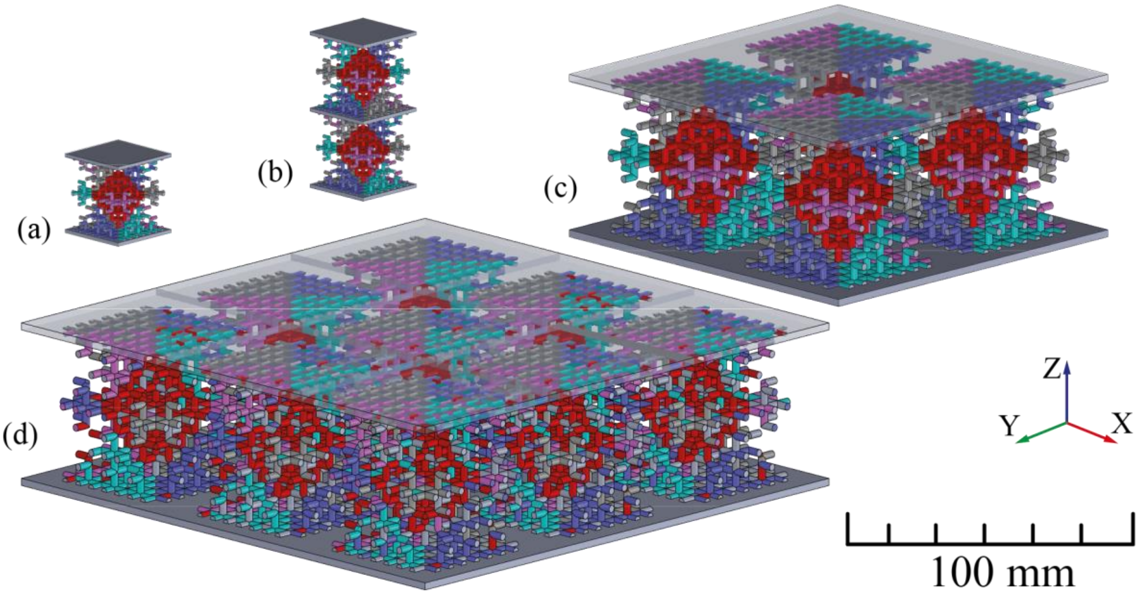

Fig. 6. Configuration for analysing the scale-effect configurations structure: D2_50%, D2_50%_2z, D2_2×2, D2_3×3.

Table 1. Geometrical characterisation of the tested configurations according to the diameter of the strut D, the length of the strut at the first step L, and the number of replication along the three cartesian axes.

ID	D [mm]	L_1 [mm]	Replica along X [#]	Replica along Y [#]	Replica along Z [#]

D1	1	40	1	1	1
D1.5	1.5	40	1	1	1
D2	2	40	1	1	1
D2.5	2.5	40	1	1	1
D2_50%	1	20	1	1	1
D2_50%_2z	1	20	1	1	2
D2_2×2	2	40	2	2	1
D2_3×3	2	40	3	3	1

2.2 Production and testing

The samples were manufactured with the Formiga Velocis P110 (EOS GmbH) and recycled PA2200 powder (EOS tradename of the PA12) to simulate industrial conditions. As suggested by the supplier, the PA2200 material was used as a mixture of 50% virgin and 50% recycled powder. Table 2 reports the main properties of the material [65]. The process parameters used for the production are summarised in Table 3.

Table 2. The main material and mechanical properties of the PA2200 powder extracted by the technical datasheet [65].

Tensile modulus [MPa]	1650
Tensile strength [MPa]	48
Elongation at break [%]	18
Melting temperature [°C]	176
Bulk density [g/cm^3]	0.45
Density of laser-sintered part [g/cm^3]	0.93

Table 3. Formiga P110 Velocis process parameters for PA2200 material.

Parameter	
Process chamber temperature [°C]	172

Removal chamber temperature [°C]	154
Laser power [W]	21
Scan speed [mm/s]	2500
Hatch distance [mm]	0.25
Layer thickness [mm]	0.100
Laser spot [mm]	0.400

To properly model the mechanical properties of the material (see Section 2.3.1), tensile tests were experimentally performed using a universal testing machine AURA Easydur. The device is equipped with a 10 tonnes load cell, servo-electric actuator, and pneumatic wedge action grips. According to EN ISO 527-2:2012 [66], the crosshead speed of the tensile test was set to 5 mm/min, corresponding to a 2×10^{-3} s^{-1} strain rate. The strain data were recorded using an extensometer with a gauge length of 49 mm. The testing data were recorded with a sampling rate of 500 Hz.

For each 3D-CFS configuration, five replicas were produced. An example of the manufactured samples in different configurations is shown in Fig. 7. The plates of each sample were oriented parallel to the build platform.

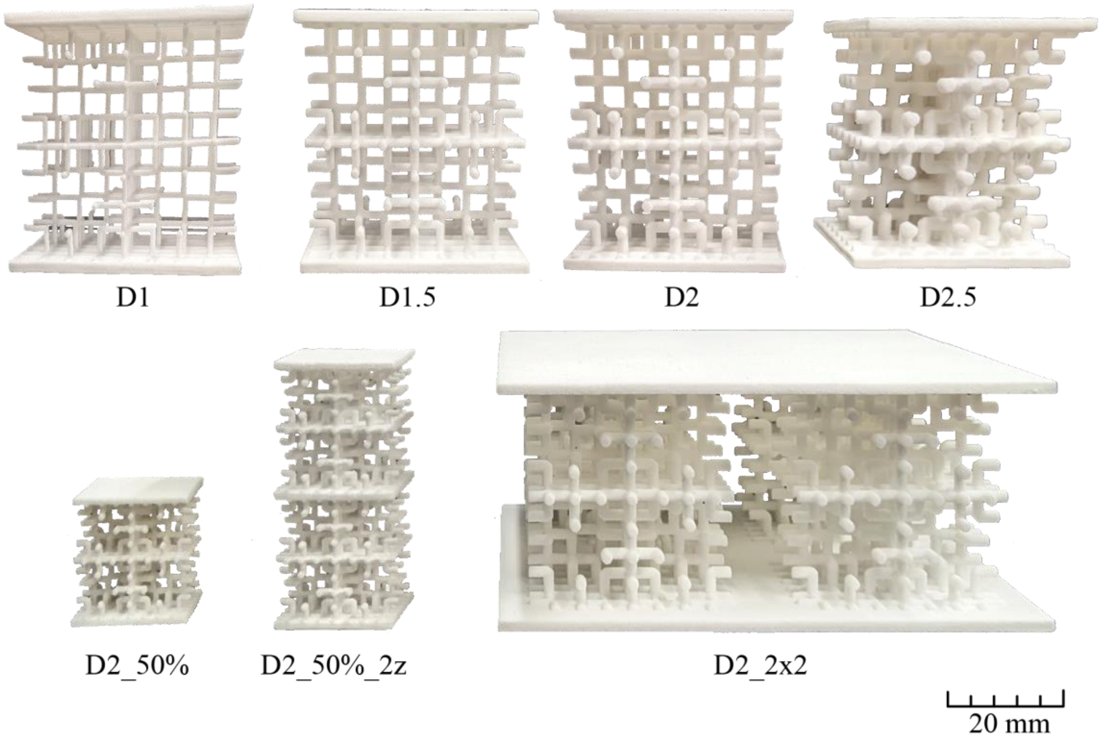

D1 D1.5 D2 D2.5

D2_50% D2_50%_2z D2_2x2

Fig. 7. 3D-CFS configuration samples produced via SLS in PA2200.

After the production, quasi-static compression tests were performed using a universal testing machine, 3MZ Easydur, equipped with a load cell of 5 tonnes. The crosshead speed for the compression tests was set to 5 mm/min. The sampling rate was equal to 100 Hz. The strain (ε_e) was calculated considering the crosshead displacement (Δl) with a gauge length equivalent to the structure height (l_0). The nominal stress was calculated as the ratio of response force (F) measured by the load cell and the nominal area of the structure (minimum cross-section A_0) extrapolated by the CAD file. Eq. 1 and Eq. 2 report the formulas used to calculate the engineering strain and stress.

$$\varepsilon_e = \frac{\Delta l}{l_0} \tag{1}$$

$$\sigma_e = \frac{F}{A_0} \tag{2}$$

The energy absorption W is commonly calculated using Eq. 3, which represents the work performed by the structure under compression until the densification of the structure. W is computed as the area under the stress-strain curve until the densification strain (ε_d) [67].

$$W = \int_0^{\varepsilon_d} \sigma(\varepsilon) d\varepsilon \tag{3}$$

However, to take into account the density of the absorber, the specific energy absorption (SEA) was also calculated according to Eq. (4) as the ratio between W and the material density [68].

$$SEA = \frac{W}{\rho} \tag{4}$$

The porosity and dimensional accuracy of the printed specimens were analysed by computed tomography scanning (CT-scan) (GE Phoenix v|tome|x s). The scans were performed using a voltage of 140 kV and a current of 180 μA. The scan magnification was set to achieve a voxel size of 0.055 mm. The projection images and the porosity analyses were performed using VGStudio Max 3.4.

2.3 Numerical simulations

The numerical tests of the 3D-CFS have been modelled and solved using the finite element (FE) method. The CAD file model was meshed using Hypermesh, and the FE model was implemented in HyperWorks 2021 (Altair®). All the numerical simulations were solved using the RADIOSS® solver.

2.3.1 Material modelling

The polyamide was modelled as an elastoplastic isotropic material. Additionally, an implicit non-linear analysis was performed to simulate better a mechanical test under quasi-static load conditions. The material model selected for the PA2200 is the elastic-plastic piecewise linear material (MAT/LAW36) [69]. The plastic curve extracted from tensile tests was implemented as input in the material model. Because of the large plastic deformation before the failure point of the polyamide, the engineering stress-strain curve was converted into a true stress-strain curve using Eq. 5 and Eq. 6. Considering the non-linear behaviour of the material, the beginning of the plastic field (yield point) was assumed as the true stress value corresponding to 0.2% true strain. Then, the plastic strain was computed using Eq. 7 within the range of the yield point and the maximum stress value. The obtained true stress versus yield-strain curve was implemented as material law in the FE software.

$$\varepsilon_{\mathrm{tr}} = \ln(1 + \varepsilon_{\mathrm{e}}) \tag{5}$$

$$\sigma_{\mathrm{tr}} = \sigma_{\mathrm{e}} \cdot \mathrm{e}^{\varepsilon_{\mathrm{tr}}} \tag{6}$$

$$\varepsilon_{\mathrm{pl}} = \varepsilon_{\mathrm{tr}} - \frac{\sigma_{\mathrm{tr}}}{\mathrm{E}} \tag{7}$$

The mechanical properties of the material for the numerical model calibration were obtained by testing dog-bone specimens (Fig. 8a) designed according to EN ISO 527-2:2012 [66] and the related local reference system (LRS). The samples were printed along three orientations, as summarised in Fig. 8b. In the flat position, the larger specimen cross-section is located on the XY plane of the LRS and is parallel to the build platform. In the edge position, the sample cross-section lying on the ZX plane is parallel to the build platform, that is, the flat orientation, which is rotated 90 degrees along the X-axis of the LRS. In the vertical position, the X axis of the LRS is along the build direction; consequently, the smallest cross-section is parallel to the platform. Five replicas were fabricated for each orientation and tested by a uniaxial tensile test.

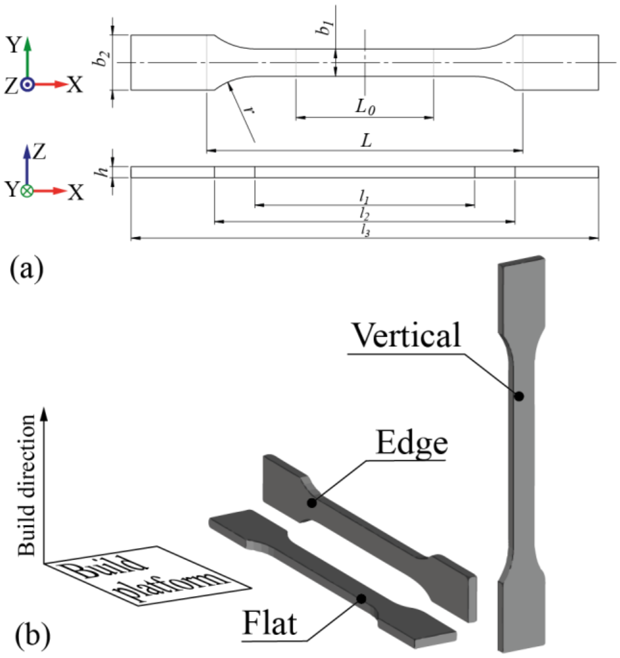

Fig. 8. (a) Geometric dimensions of type 1A specimen (EN ISO 527-2:2012) [66]; (b) flat, edge and vertical orientations in the build volume.

Table 4. Geometric values of type 1A specimen of Fig. 8a (EN ISO 527-2:2012) [66].

l_3	Overall length	170	[mm]
l_1	Length of narrow parallel-sided portion	80 ± 2	[mm]
r	Radius	24 ± 1	[mm]
l_2	Distance between broad parallel-sided portions	109.3 ± 3.2	[mm]
b_2	Width at ends	20.0 ± 0.2	[mm]
b_1	Width at narrow portion	10.0 ± 0.2	[mm]
h	Thickness	4.0 ± 0.2	[mm]
L_0	Gauge length	50.0 ± 0.5	[mm]
L	Initial distance between grips	115 ± 1	[mm]

The tensile modulus was set equal to the average value obtained by the experimental tensile test. According to the material datasheet, density and Poisson ratio were set equal to 0.93 g/cm^3 and 0.39, respectively. To validate the developed material model, the tensile test was modelled and simulated in RADIOSS. The dog-bone specimen was discretised by four-node tetrahedral elements (TETRA4). After a convergence study, the element size of the mesh was set to 0.8 mm. Load conditions were applied on the surface nodes of the specimen ends. The first end was fixed in all the degrees of freedom (DoF), whereas on the second one, a constant velocity of 0.083 mm/s, which is equivalent to the 5 mm/min of the tensile test, was imposed. In addition, to simulate the material failure behaviour, the failure model was activated (FAIL/BIQUAD) using a non-linear strain-based failure criterion described by a bi-quadratic function [70]. This model requires as input the plastic failure strain value obtained experimentally by different load conditions. The failure model was calibrated by varying the failure coefficient and comparing the experimental results with the numerical curve.

2.3.2 Compression test modelling

The compression test was simulated by setting a non-linear quasi-static implicit analysis in the large displacement field. A self-contact interaction was applied among the struts with a friction coefficient equal to 0.3. The 3D-CFS structure was discretised by four-node tetrahedral elements (TETRA4) with an adaptive element size ranging between 0.2 mm and 6 mm. The actual mesh size depended on strut diameter dimension and SLS process resolution. However, the ratio between the strut diameter and the number of elements in the strut cross-section was kept almost constant and ranged between 0.2 mm and 0.3 mm. The compression was simulated by imposing a speed of 0.083 mm/s to a node connected rigidly to the top surface of the top plate. Moreover, the top plate was constrained to move only along the load direction, while the bottom plate was fully constrained.

The D2_3×3 was analysed numerically only, and the compression load was applied in a restricted area of the top base. This load configuration emulates shock impacts applied in restricted areas of crash helmets during real-life accidents and, therefore, the energy absorption performance of a single cell bonded to adjacent cells.

2.3.3 Impact test modelling

The mechanical behaviour of the 3D-CFS cell under shock impact load has been investigated using explicit numerical analysis. As an example of the structure shock-absorption properties, the impact speed was set as defined by the ECE 22.05 standard according to the use of the structure in a motorcycle helmet [71]. According to the ECE 22.05 standard, the drop-tested helmet must reach a prescribed minimum energy absorption value when the impact occurs at a speed value of 7.5 m/s. Therefore, 7.5 m/s was set as an instant velocity in the model. The simulation time was set to 40 ms. As a preliminary analysis, the failure model was not considered.

2.3.4 Modelling summary

The main parameters set used in the FE analysis are summarised in Table 5. The methodology used to develop the current experimental and numerical work is described in the flowchart reported in Fig. 9. The crucial part is the definition of the material modelling, which should consider the peculiarity of the material production at a microscopic level.

Table 5. FE model parameters used in this work for the different load conditions.

	Tensile test	Compression test	Impact test
Analysis mode	• Non-linear • Quasi-static • Implicit • Large displacement	• Non-linear • Quasi-static • Implicit • Large displacement	• Non-linear • Dynamic • Explicit • Large displacement
Solver	RADIOSS	RADIOSS	RADIOSS
Material LAW	Elasto-plastic LAW36	Elasto-plastic LAW36	Elasto-plastic LAW36
Failure mode	FAIL/BIQUAD	FAIL/BIQUAD	-

Mesh	TETRA4	TETRA4	TETRA4
Element size [mm]	0.8	0.2-6	0.2-6
Imposed velocity [mm/s]	0.083	0.083	7500
Simulation time [s]	200	300	40×10^{-3}

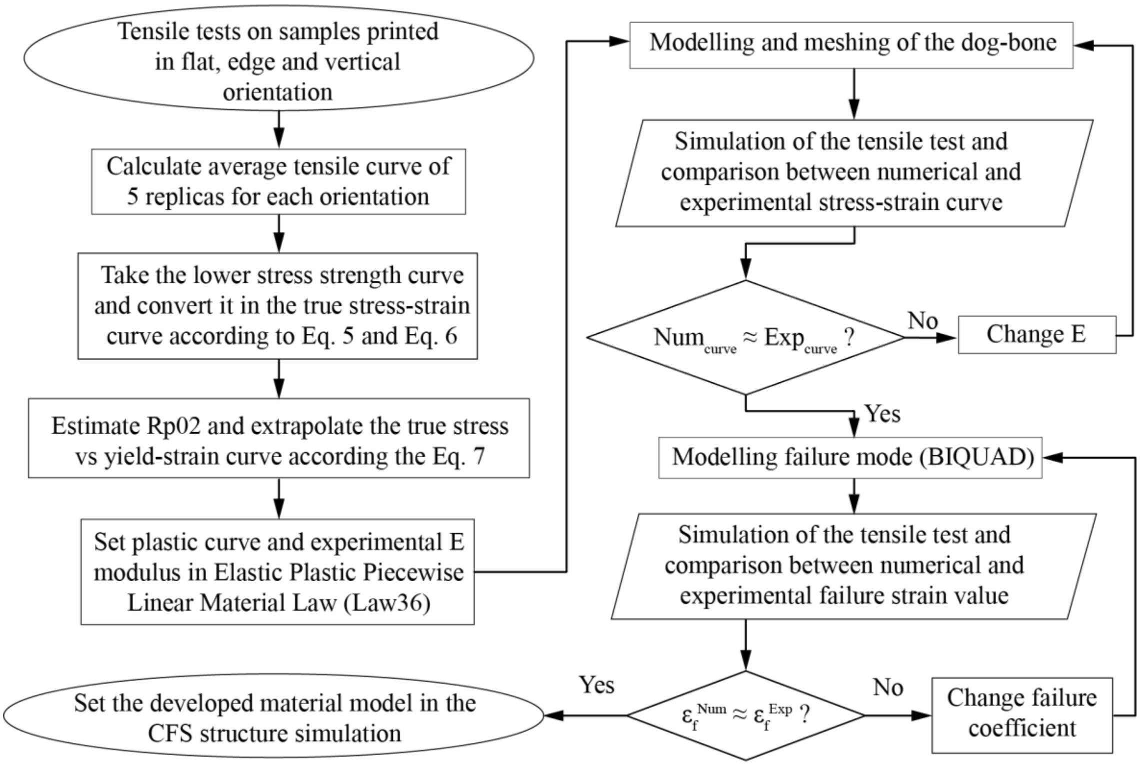

Fig. 9. Flowchart for modelling the material properties from the current experimental test.

3 Results and discussion

3.1 Material characterisation

The stress-strain curves of the PA2200 bulk sample replicas have statistically confirmed the Young’s modulus (E) value reported in the EOS datasheet. The samples produced in flat and edge positions are characterised by E values of 1656 MPa ± 81.6 MPa and 1643 MPa ± 52.7 MPa, respectively. The samples printed along the building direction (

vertical) showed a lower tensile modulus of 1013 MPa ± 43.9 MPa. These differences agree with the results reported in Ref. [72]. The average stress-strain curves obtained from the experimental samples are reported in Fig. 10a. The curve of the flat specimens presents higher tensile strength and elongation values than the edge counterpart. The curve of the vertical specimen shows different behaviour in the plastic region, and the tensile strength values before the fracture were higher than the flat and edge counterparts. Overall, it can be observed that for the same strain values, the edge dog-bone sample presents lower values of stress. This deviation can be explained by the presence of internal porosities for which the distribution and the quantity depend on the size, shape and orientation of the component [72].

As a preventive measure, the curve with lower ultimate tensile strength values and weakest plastic behaviour, i.e. the edge-oriented sample curve, was selected to characterise the material model in RADIOSS. The true stress-strain curve for the edge specimen is reported in Fig. 10b. A good match between the experiments and the numerical simulation has been detected with a mesh size corresponding to 0.8 mm (Fig. 11).

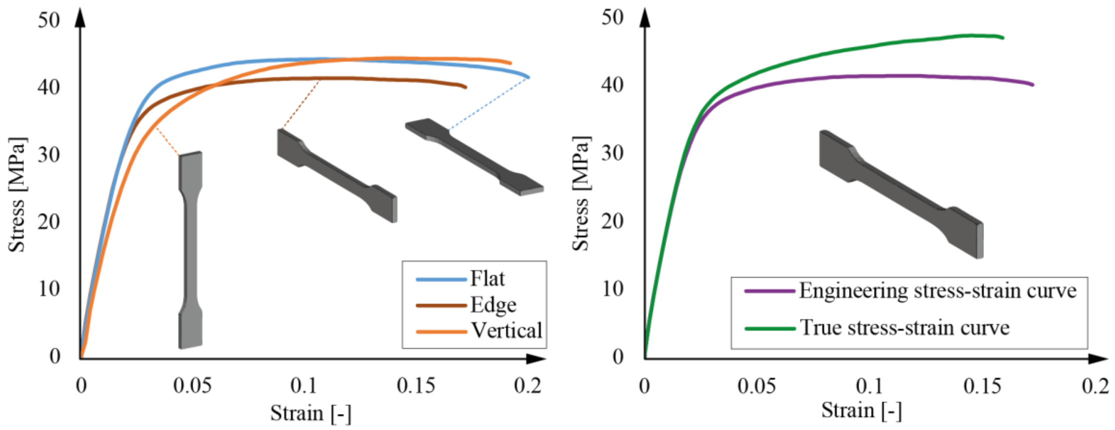

(a) (b)

Fig. 10. (a) Comparison between average engineering stress-strain curve of flat, edge and vertical-oriented samples; (b) the engineering and true stress-strain curve of the edge-oriented sample.

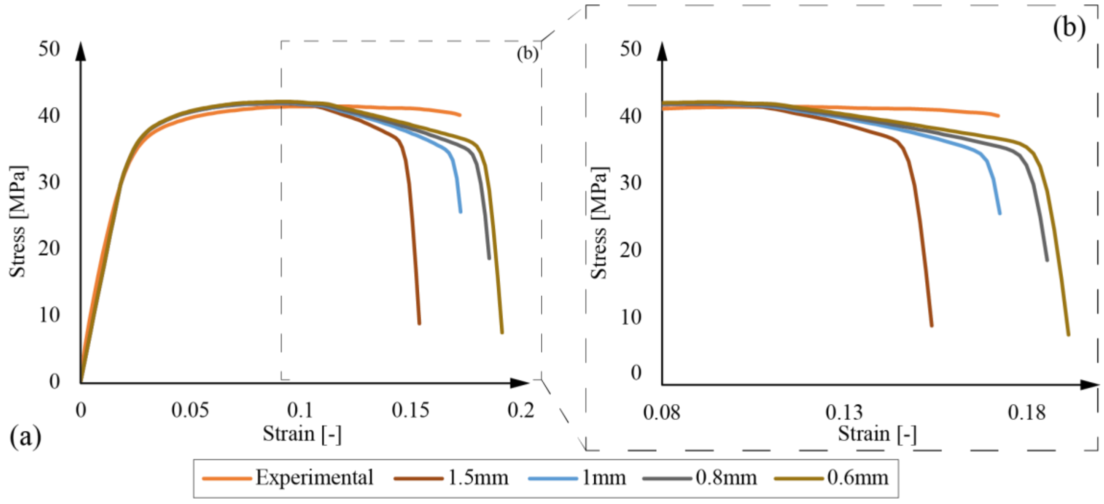

Fig. 11. (a) Material numerical model: mesh element size convergence. (b) Detailed graph in the 8-20% strain range.

3.2 Diameter effect

The variation of the strut diameter was analysed by maintaining the cubic envelope of 40 mm and the third fractal iteration. The experimental results of the compression test on the fractal structures with different strut diameters are shown in Fig. 12. The variation of the strut diameter linearly reduces the structure stiffness. However, by comparing the first peak of the curves, there is a higher decrease in the strength of the 1 mm diameter 3D-CFS structure. This result can be explained by a more significant effect of the defect generated during the manufacturing of the samples. The differences in the elastic behaviour of the structure can be better appreciated in Fig.12b and Table 6. As it can be observed, the Young’s modulus decreases significantly by decreasing the diameter of the structure. In particular, the Young’s modulus value drops for the structure with a diameter equal to 1 mm. As mentioned above, this result may be explained by considering a more remarkable effect of the process-induced defects (porosities and shape of the strut) on the mechanical performance of the structure. As an example, Fig. 13 compares sections of D1 and D2 specimens obtained by CT scan analysis. The presence of multiple internal porosities can be detected in both D1 and D2 struts. Even if in fewer numbers, the porosities in the thinner structure appear to be less circular and bigger. The printed struts along and perpendicular to the build direction show an average diameter size of 0.93 ±0.25 mm and 1.88 ±0.23 mm for the D1 and D2 specimens, respectively, which is comparable with the nominal counterparts. However, the horizontal struts of the D1 specimen present a significant shape deviation from the nominal circular cross-section (Fig. 13b).

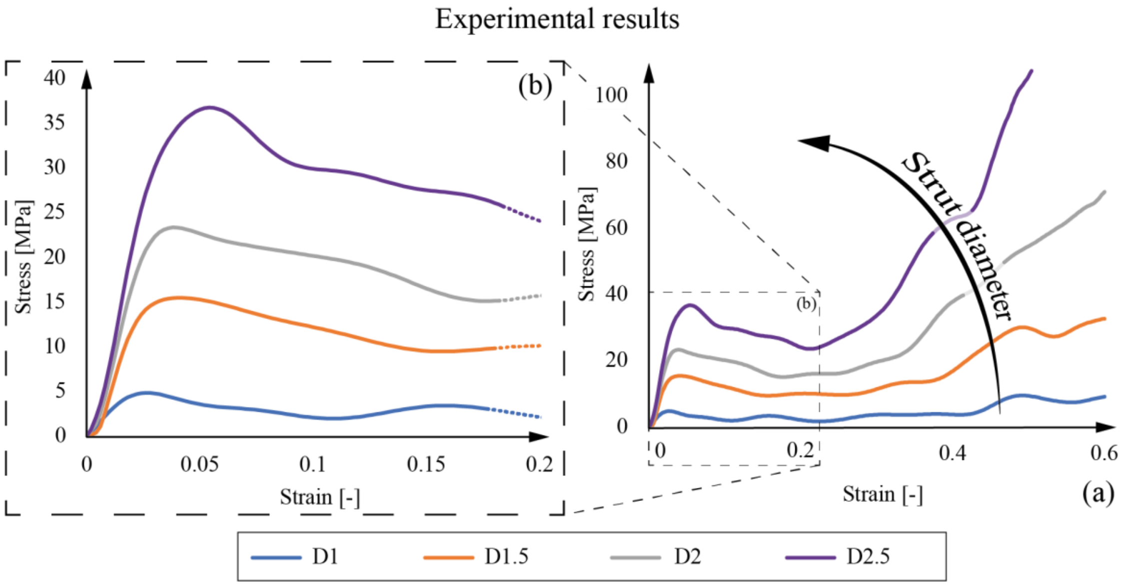

Fig. 12. (a) Experimental stress-strain curve of 3D-CFS specimens with a different strut diameter; (b) detailed graph in the 0-20% strain range.

Table 6. Comparison between Young's modulus evaluated experimentally (E_{exp}) and numerically (E_{num}). The E_{exp} represents the mean value with the corresponding standard deviation of the five replicas for each configuration.

	E_{exp} [MPa]	**E_{num} [MPa]**
D1	274 ±42	544
D1.5	922 ±66	851
D2	1101 ±70	1474
D2.5	1373 ±3	1449

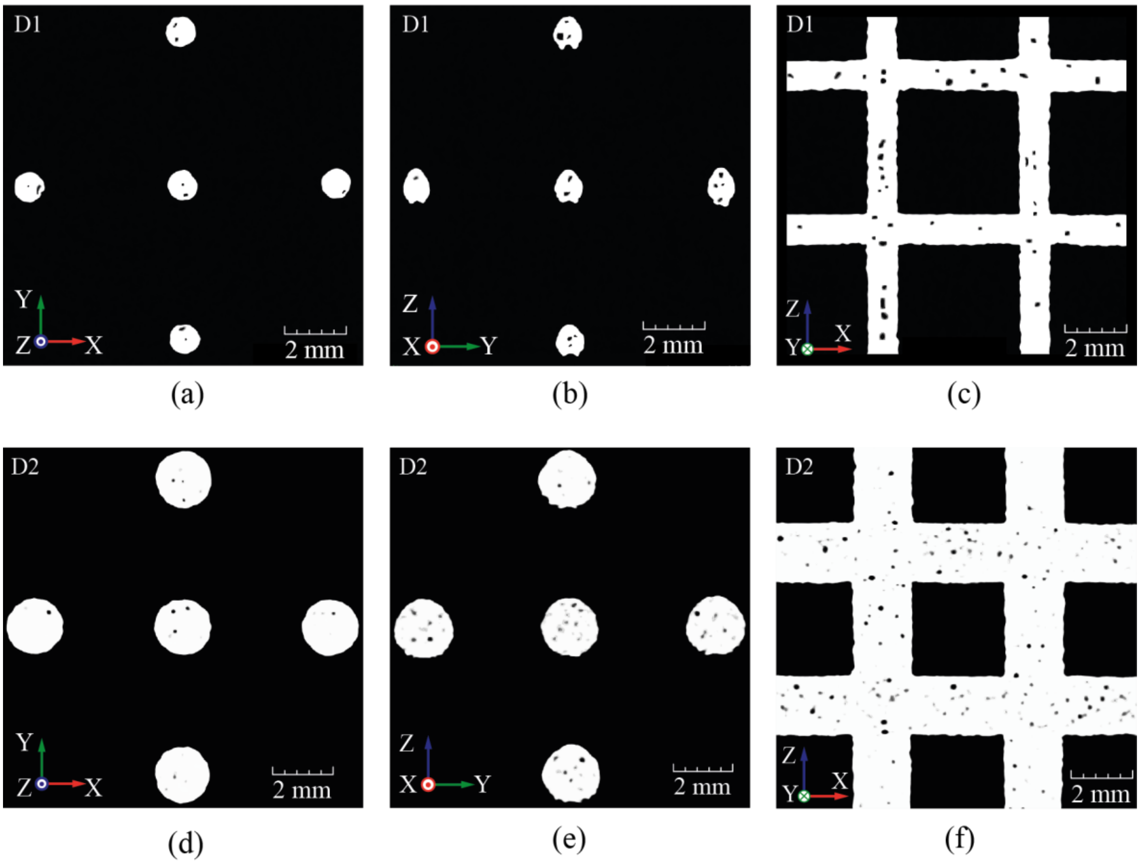

Fig. 13. CT-scan images of D1 (top) and D2 (bottom) specimens in different cross-sections. The pores are visible in black. (a)-(d) Y-X plane-section of the vertical struts; (b)-(e) Z-Y plane-section of the horizontal struts; (c)-(f) Z-Y plane-section at the middle position of the struts.

The 3D-CFS structures compression test simulations were performed both neglecting (Fig. 14a) or considering the strut damage or break (Fig. 14b). The failure mode (Fig. 14b) was implemented because of the fracture of the structure in a few localised nodes observed experimentally at around 5% of strain. These fractures induce a rapid decrease in the strength of the structure and, consequently, a fragmentation of the plateau region. In addition, the non-localised fracture can lead to an asymmetry bending behaviour of the structure and different load distribution among the struts.

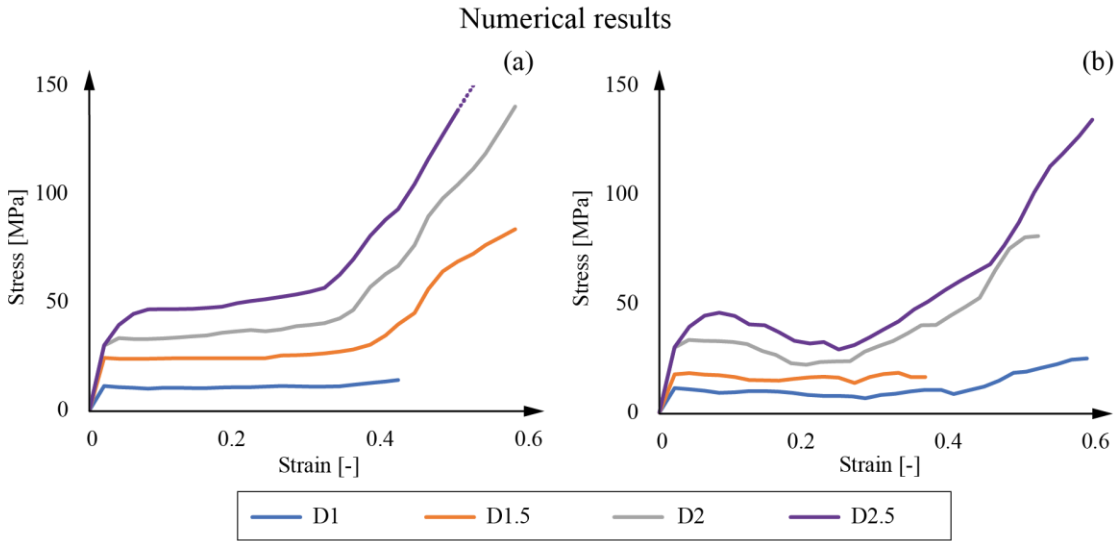

Fig 14. Numerical stress-strain curve of 3D-CFS with different strut diameters: (a) numerical analysis without implementation of the failure mode (b) numerical analysis without implementation of the failure mode.

The differences between the implemented numerical models compared to the experimental results for each 3D-CFS structure are highlighted in Fig. 15. Both models overestimate the mechanical behaviour of the structure, meaning that the material model is stiffer than the actual material. However, the model with the activation of the failure mode can better predict the bending behaviour of the struts and the related fractures. In contrast, the model with no failure mode reports a constant plateau with a higher densification strain.

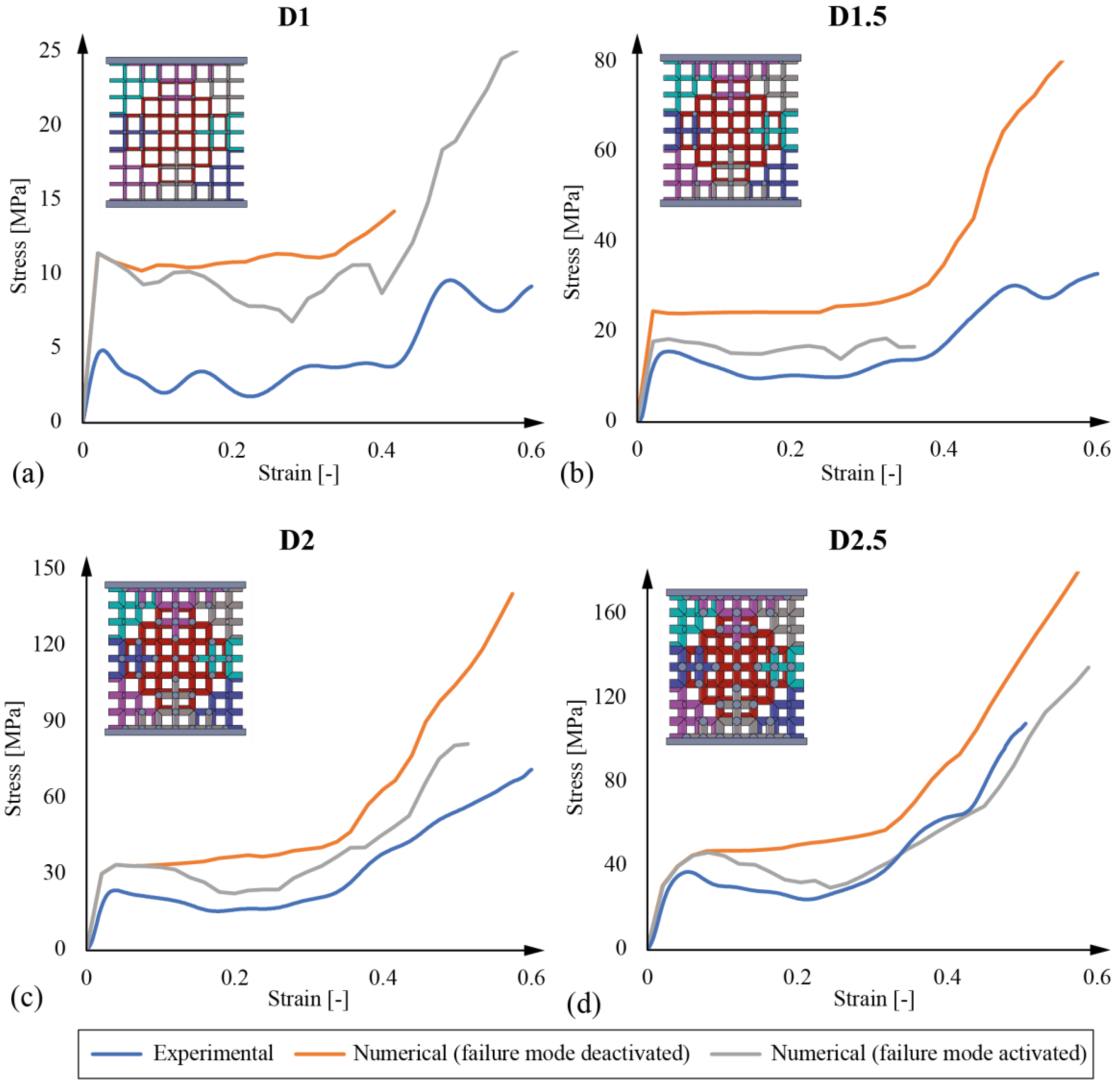

Fig. 15. Comparison between the experimental and numerical results of the 3D-CFS structure with different diameters: (a) D1, (b) D1.5, (c) D2, (d) D2.5.

In terms of Young's modulus, overall, the numerical results agree with the experimental counterpart (Table 6), where a decrease in the diameter corresponds to a decrease in the structure stiffness. The deviation between the numerical and the experimental values could be explained by the fact that internal porosities, roughness or deviation from the nominal dimension related to the structure's shape (Fig. 13) have been neglected in the model and can hardly be considered in the modelling. In fact, the most remarkable result deviation is detected in D1. As regards the deformation mechanism, as an example, Fig. 16 shows the numerical and experimental deformation of the D2 sample structure at four different strain levels, with the associated stress level. As it can be observed, the numerical model emulates well the structure deformation. In terms of stress, the deviation between the experimental and numerical results is constant during the test indicating a systematic effect that may be neglected in the modelling.

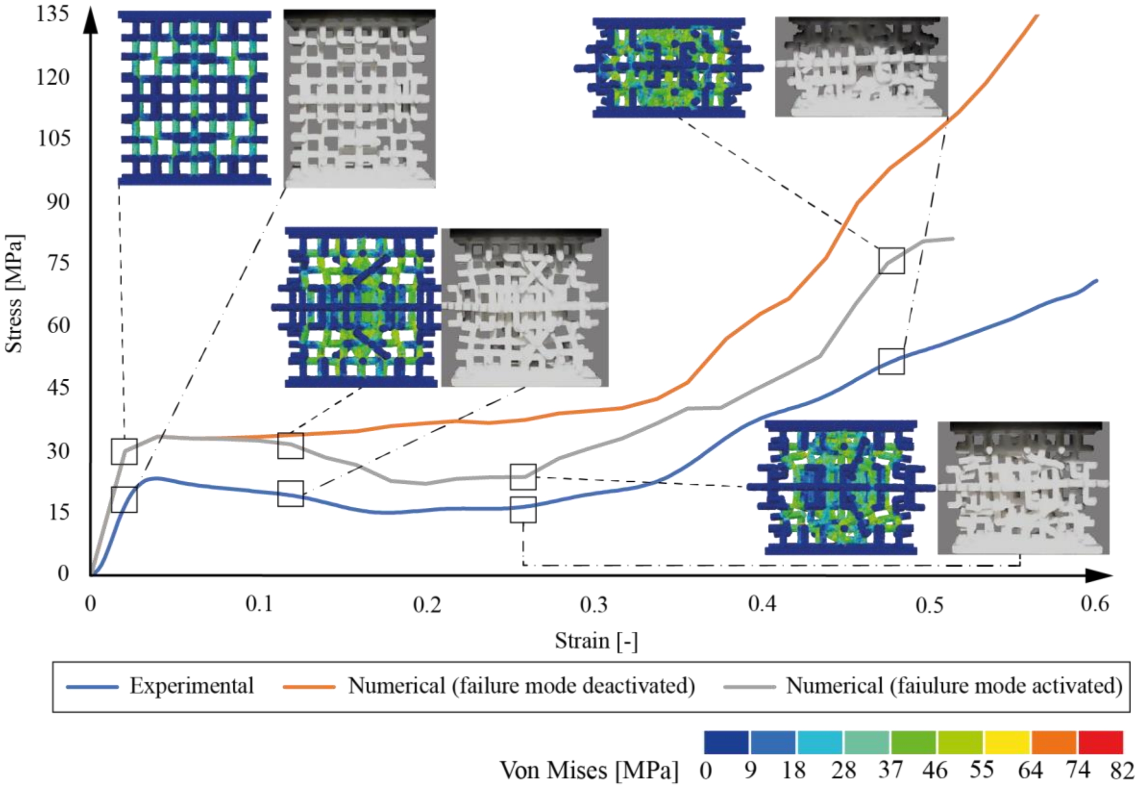

Fig. 16. Comparison between the experimental and numerical results of the D2 with its four different strain levels frame. The animation of the experimental deformation in comparison with the numerical counterpart is provided as supplementary material.

The simulation of the compression test shows that the higher stresses are localised in the horizontal and vertical-oriented struts because of the combination of more deformation mechanisms. The external vertical struts bend with a bell-shaped curve along the compression load (highlighted by the dotted red line in Fig. 17). This deformation is combined with a torsion around the Z axis of the central fractal structure with higher rotation degrees at the centre group of struts (Fig. 17). The torsion deformations allows for the creation of a wider plateau region of the stress-strain graph and a more controlled compression. The structure reaches a rotation up to about 45° in the middle before the starting of the densification phase (cross-section A-A in Fig. 17). By considering constant the L value of 3D-CFS, higher values of diameter size increase the stiffness of the structure, because the reduction of the torsion deformation and the increasing of the stress around the nodes leading to premature fractures.

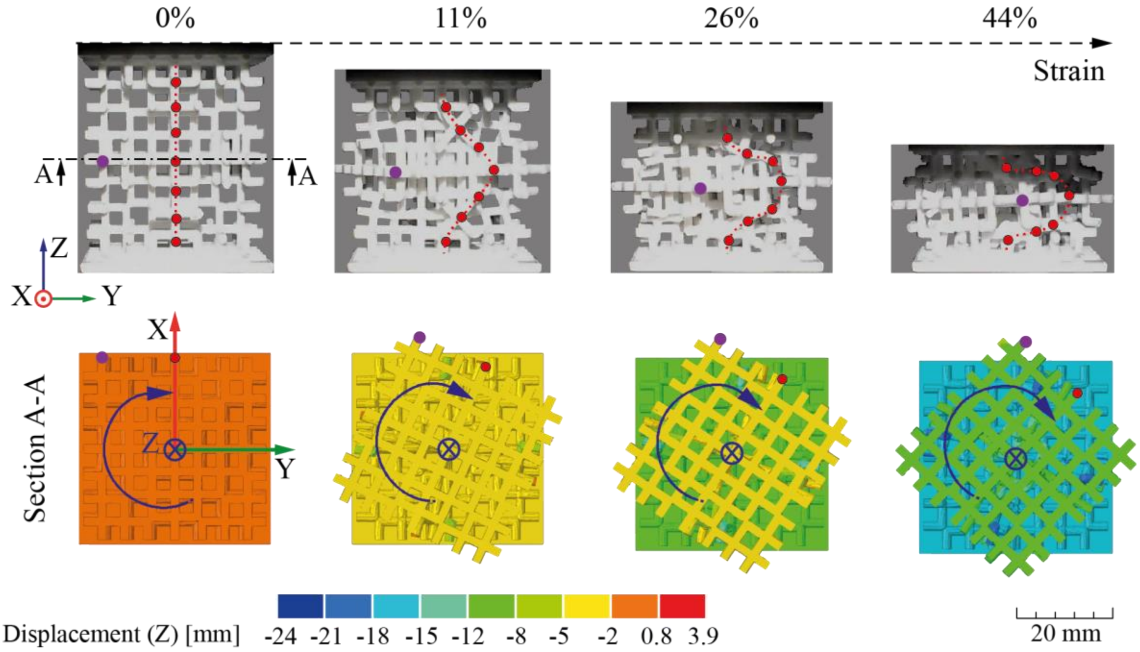

Fig. 17. Deformation mechanisms. In the top, experimental deformation up to 44% of strain for the D2 structure; the dotted red line represents the bending of the external vertical struts, which assumes a bell-shaped curve along the compression. Section A-A reported in the bottom, extrapolated by the FE model, highlights the corresponding torsion deformation of the structure up to 45° of rotation around the Z axis.

3.3 *Multi-cell and scale effect*

The adaptation of the structure to a specific design was analysed by investigating the mechanical behaviour of the D2 structure in scaled and multi-cell configurations. In this case, the experimental stress-strain curves of a 50% scaled structure (D2_50%) and two multiple cells arranged along the Z-axis and in the XY plane (D2_50%_2z and D2_2×2) are compared in Fig. 18 with the initial configuration D2. Even if all configurations present the same volume fraction, the experimental results confirmed the systematic decrease of mechanical performance for SLS components manufactured with minimum features of about 1 mm (D2_50% and D2_50%_2z). These structures present a Young's modulus of 391 ±14 MPa and 446 ±25 MPa, respectively. These values agree with the previous results obtained for the D1 structure. However, the different cell dimension, which corresponds to a higher volume fraction than D1, results in a higher E value.

The structure arrangement in the space does not significantly affect its performance. As an example, Fig. 19 shows the deformation mechanisms of the D2_50%_2z. As can be observed, the deformation in terms of bending and torsion is similar to the single cell (Fig. 17). Under compression, the torsion of the structure is transferred from one structure to the adjacent by the central plate, which is free to rotate and translate under the bending deformation of the adjacent struts. Initially, the central plate starts rotating around the Z axis and parallelly to the compression plate. Further rotations and translations occur because of asymmetric bending and fractures of struts. These phenomena drastically reduce the mechanical strength of the structure and accentuate the asymmetry of the bell-curve emulated by the dotted red line.

Comprehensively, the configurations with the same strut diameters exhibit similar mechanical strength values. These findings prove that, with some manufacturing limitations, the designed structure can be scaled and rearranged in different configurations without appreciable variation from the elementary cell properties.

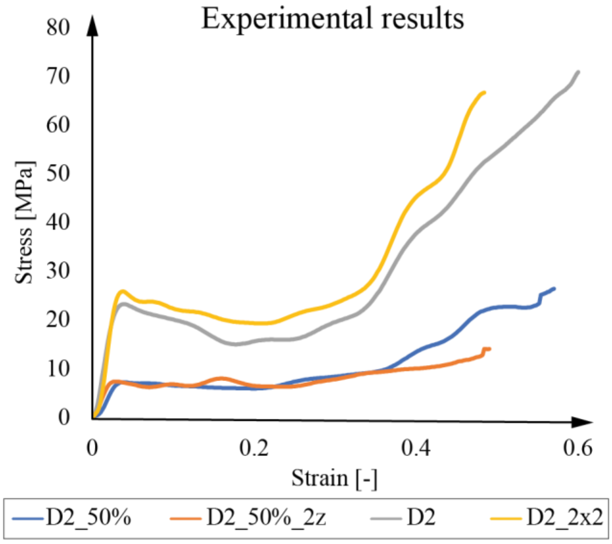

Fig. 18. Experimental stress-strain curves of D2 structure with different scales and multi-cell combinations.

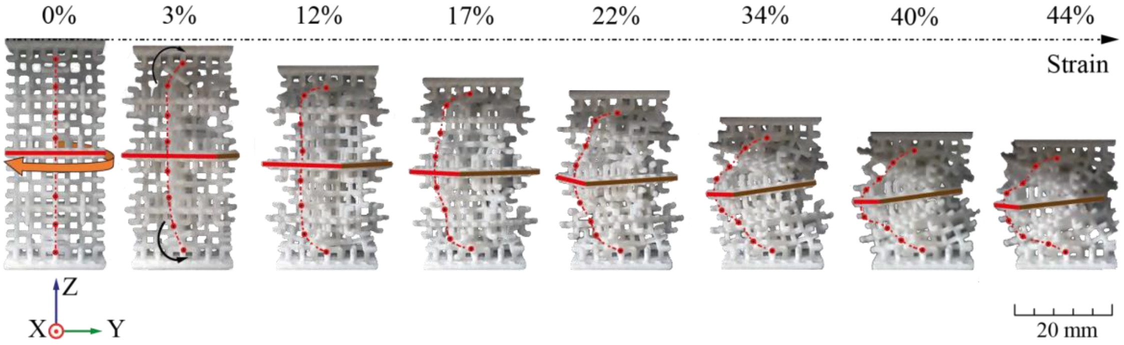

Fig. 19. Deformation mechanism of D2_50%_2z structure. The images depict the experimental deformation up to 44% of strain; the dotted red line represents the bending of the external vertical struts, which assumes a bell-shaped curve along the compression. The red and brown straight lines represent the edge of the middle plate. These lines highlight the torsion deformation of the structure around the Z axis.

Comparing the numerical and experimental results, the most significant deviation is still detected in the case of thinner structures (Fig. 20). Configurations with the same diameter show almost a constant deviation. The systematic deviation between the simulated and experimental parts reveals a systematic influence of the manufacturing process on the mechanical performance of the structure.

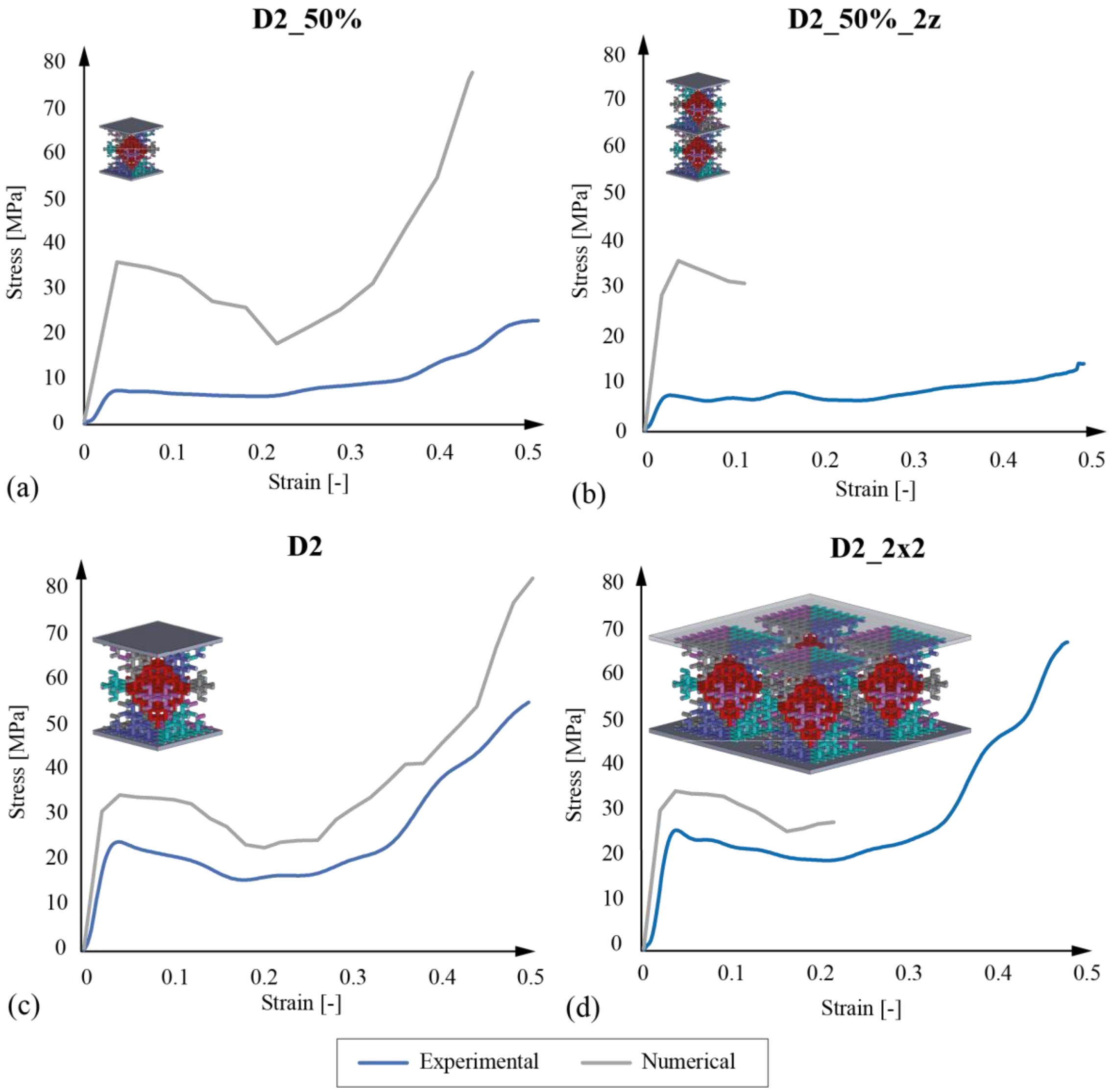

Fig. 20. Comparison between the experimental and numerical results of the D2 structure with different scales and multi-cell combinations: (a) D2_50%, (b) D2_50%_2z, (c) D2, (d) D2_2×2.

The mechanical behaviour of the D2_3×3 structure under a localised load was analysed via FE only (Fig. 21). Compared to the D2 structure under the same load conditions, the multi-cell has a higher value of response in terms of force. However, the plateau region is shorter (Fig. 21a). This reduction may cause higher peak acceleration values during high-speed shock loads.

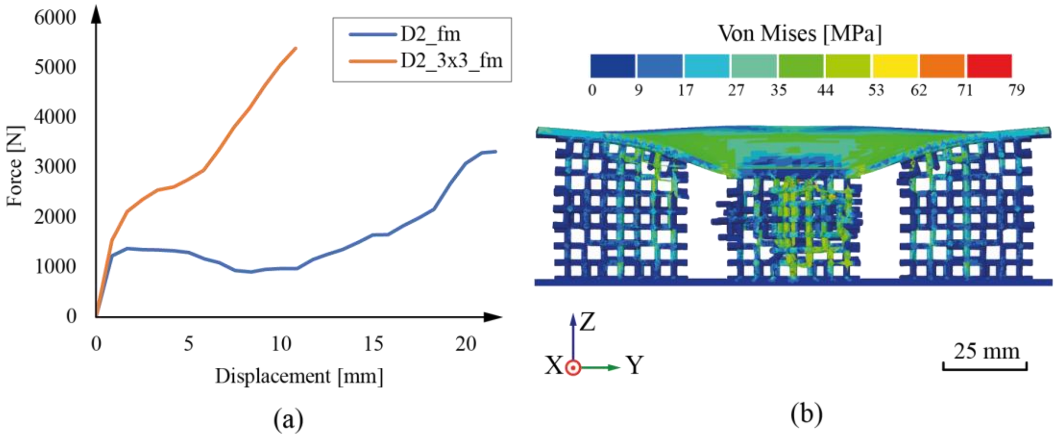

Fig. 21. (a) Force-displacement curve of D2 compared with D2_3×3 modelled with failure mode. (b) Cross-section of D2_3×3 under compression.

3.4 Impact test results

In this paragraph, the stress-strain graph of the D2 structure numerically tested under high-speed (HS) impact load (7.5 m/s), named D2_HS, is compared with the same structure under quasi-static (QS) compression load (8.3×10^{-2} m/s), named D2_QS (Fig. 22a). The high strain rate value mainly influences the mechanical behaviour of D2_HS with dynamic loads, which prevents the fully bending deformation of the struts. As a result, higher stress values are generated, mainly localised around the reticular nodes and on the struts extruded along the Z-axis, which belong to the first fractal step (Fig. 22b). The response of the structure under impact load is excellent. It presents higher mechanical properties than the D2 structure under quasi-static compression load. This result means a higher amount of energy absorption.

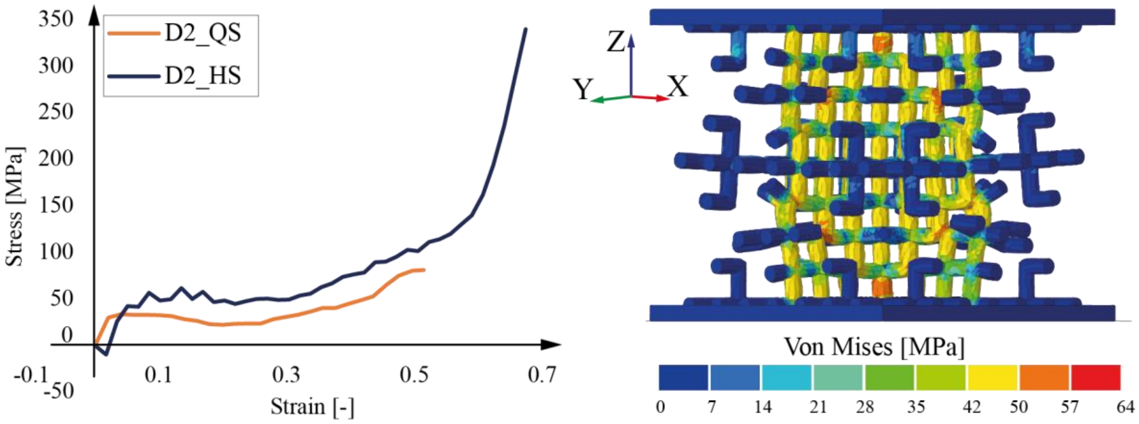

Fig. 22. (a) Numerical comparison between D2 structure test under compression load versus impact load. (b) Von Mises stress distribution on D2_HS model.

3.5 Energy absorption performance

The response in terms of energy absorption (W) against the strain of the D2 structure analysed under different speeds of compression load was investigated and reported in Fig. 23. D2_HS reached a total energy absorption 50% higher than the D2_QS. This marked behaviour of the 3D-CFS may suggest a good adaptation of the structure for head protection equipment. To evaluate the applicability in this field, the energy absorption performance of the 3D-CFS is compared with one of the most commonly adopted materials, expanded polystyrene foam EPS-60.

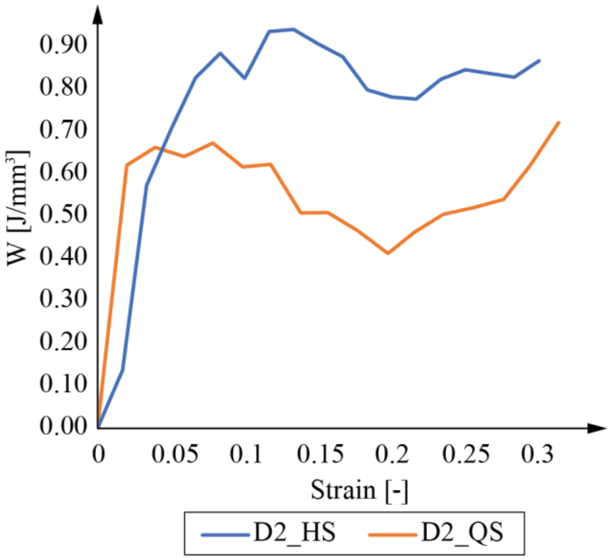

Fig. 23. Comparison between the D2_HS and D2_QS of the variation of the energy absorption (W) with the strain up to the assumed densification strain.

The strain-stress curve under quasi-static compression load of expanded polystyrene foam EPS-60, extracted from literature [73], is reported in Fig. 24a and compared in Fig. 24b with the 3D-CFS counterpart. As can be observed, the areas under the stress-strain curves obtained from the different materials are significantly different (Fig. 24b). This difference is strictly correlated with the material densities (see Table 7), which makes the results difficult to compare. Because of that, the SEA value can be used as a more reliable indicator to compare the structures. The SEA value for each structure was calculated according to Eq. 4 (Section 2.2) and reported in Table 7. The total energy ($W_{\varepsilon=30\%}$) was calculated up to initiating the densification area (assumed 30% strain).

Remarkably, the 3D-CFS structure analysed in this work can absorb up to 77% more energy with respect to the typical EPS foam. These values of energy absorption, which characterise the proposed structure, are also higher than the hierarchical lattice such as the one proposed by S. Farajzadeh Khosroshahi et al. [57] and produced in PA12 via FDM.

Table 7. Energy absorption performance comparison between EPS-60 foam, D2_QS, and D2_HS.

		EPS-60 foam	D2_QS	D2_HS
$\boldsymbol{\rho}$	$[\mathrm{kg/m^3}]$	60	930	930
$\mathbf{W}_{\boldsymbol{\varepsilon}=\mathbf{30\%}}$	$[\mathrm{J/mm^3}]$	0.21	9.4	14.1
SEA	[kJ/kg]	3.5	10.1	15.2

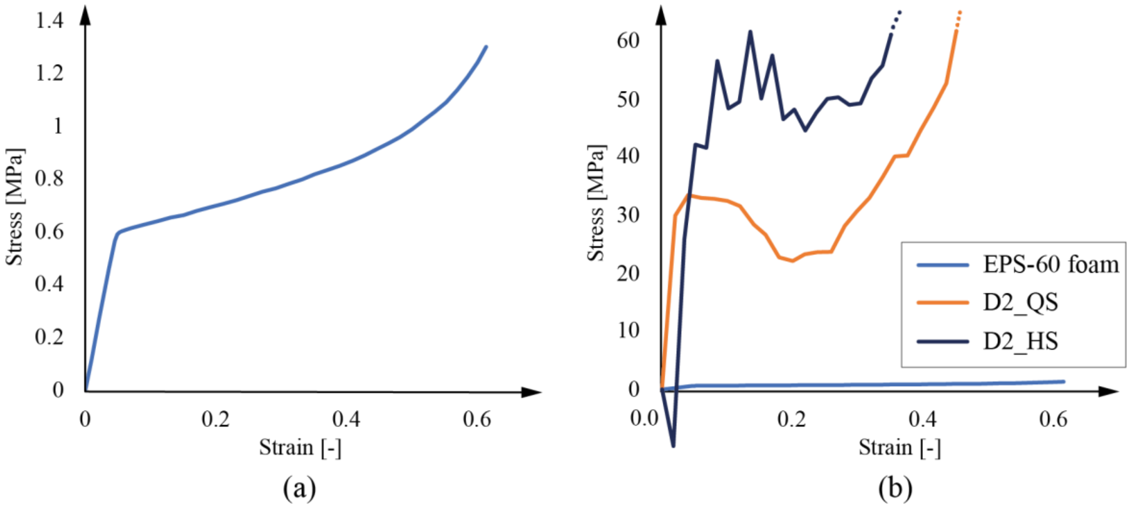

Fig. 24. (a) Stress-strain curve of EPS-60 foam [73]. (b) Comparison between EPS-60 foam and D2 CFS structure tested under quasi-static compression load.

The SEA 3D-CFS was also evaluated by varying the strut diameter. The SEA was calculated until the densification strain on the experimental average curve of the samples tested under a quasi-static compression load. The results are reported in Table 8. Except for D1, the SEA values are relatively high, and their increase can be explained by the variation of the structure stiffness by increasing the diameter.

Table 8. SEA of the experimental samples with different diameters tested under a quasi-static compression load.

		D1	D1.5	D2	D2.5
SEA	[kJ/kg]	1.3	4.2	6.1	9.7

Conclusion

In the present work, a three-dimensional cross-based fractal structure was designed for impact absorption applications and the SLS additive manufacturing technique. The structure was produced in PA2200 material. Various configurations and sizes were investigated to evaluate the effect of diameter, scale and multi-cell arrangement. A FE model was developed to numerically simulate the designed mechanical behaviour of the structure under quasi-static and dynamic compression loads. The comparison with experimental results showed a constant deviation which has been attributed to process-induced defects present in the produced material and analysed by CT-scan. This effect is more pronounced in components with minimum features below about 1 mm, for which the mechanical properties of the structure were drastically lower. The FE model showed good scalability of the 3D-CFS structure and an excellent energy absorption performance, which has been quantified as equal to 77% higher than a typical EPS-60 foam used for head protection equipment. These findings suggest a remarkable result of combining three-dimensional cross-based fractal design with additive manufacturing processes in head impact protection equipment applications.

References

[1] Peitgen, H.-O., H. Jürgens, D. Saupe, Chaos and fractals: new frontiers of science, Springer Science & Business Media, 2006.

[2] Mandelbrot, B.B., Les objets fractals: forme, hasard et dimension, (1975).

[3] Barnsley, M.F., Fractals everywhere, Academic press, 2014.

[4] OLÓRIZ, F., P. PALMQVIST, J.A. PÉREZ-CLAROS, Shell features, main colonized environments, and fractal analysis of sutures in Late Jurassic ammonites, Lethaia. 30 (1997) 191–204.

[5] Losa, G.A., Fractals in biology and medicine, Rev. Cell Biol. Mol. Med. (2006).

[6] Mandelbrot, B., How long is the coast of Britain? Statistical self-similarity and fractional dimension, Science (80-.). 156 (1967) 636–638.

[7] Camargo, S., S.R. Lopes, R.L. Viana, Extreme fractal structures in chaotic mechanical systems: Riddled basins of attraction, J. Phys. Conf. Ser. 246 (2010). https://doi.org/10.1088/1742-6596/246/1/012001.

[8] Ehret, A.E., M. Hollenstein, E. Mazza, M. Itskov, Dynamical characterization of mixed fractal structures, 6 (2011).

[9] Soo, S.C., K.M. Yu, W.K. Chiu, Modeling and fabrication of artistic products

based on IFS fractal representation, CAD Comput. Aided Des. 38 (2006) 755–769. https://doi.org/10.1016/j.cad.2006.04.003.

[10] Majewski, M., A tutorial on the realistic visualization of 3D Sierpinski fractals, Comput. Graph. 22 (1998) 129–142. https://doi.org/10.1016/S0097-8493(97)00088-5.

[11] Martyn, T., Realistic rendering 3D IFS fractals in real-time with graphics accelerators, Comput. Graph. 34 (2010) 167–175. https://doi.org/10.1016/j.cag.2009.10.001.

[12] Encarnação, J.L., H.-O. Peitgen, G. Sakas, G. Englert, Fractal geometry and computer graphics, Springer Science & Business Media, 2012.

[13] Alia, M., K. Suwais, Improved steganography scheme based on fractal set, Int. Arab J. Inf. Technol. 17 (2020) 128–136. https://doi.org/10.34028/iajit/17/1/15.

[14] Zhao, H., Q. Wu, Application study of fractal theory in mechanical transmission, Chinese J. Mech. Eng. (English Ed. 29 (2016) 871–879. https://doi.org/10.3901/CJME.2016.0818.094.

[15] Gong, Y., J. Shen, W. Liu, L. Chen, Fractal characteristics of mechanical interface contact parameters, MATEC Web Conf. 175 (2018) 1–5. https://doi.org/10.1051/matecconf/201817503009.

[16] Li, J.H., B.M. Yu, M.Q. Zou, A model for fractal dimension of rough surfaces, Chinese Phys. Lett. 26 (2009). https://doi.org/10.1088/0256-307X/26/11/116101.

[17] Sotillo, J.U., A.D. Lantada, Incorporation of Fractal Textures to 3D CAD: Towards an Enhanced Control of Surface Topography, Comput. Aided. Des. Appl. 12 (2015) 135–146. https://doi.org/10.1080/16864360.2014.962426.

[18] Farina, I., R. Goodall, E. Hernández-Nava, A. di Filippo, F. Colangelo, F. Fraternali, Design, microstructure and mechanical characterization of Ti6Al4V reinforcing elements for cement composites with fractal architecture, Mater. Des. 172 (2019) 107758. https://doi.org/10.1016/j.matdes.2019.107758.

[19] Niu, D., D. Huang, H. Zheng, L. Su, Q. Fu, D. Luo, Experimental study on mechanical properties and fractal dimension of pore structure of basalt–polypropylene fiber-reinforced concrete, Appl. Sci. 9 (2019) 1602.

[20] Li, Y., C. Ortiz, M.C. Boyce, Bioinspired, mechanical, deterministic fractal model for hierarchical suture joints, Phys. Rev. E - Stat. Nonlinear, Soft Matter Phys. 85 (2012) 1–14. https://doi.org/10.1103/PhysRevE.85.031901.

[21] Khoshhesab, M.M., Design, Mechanical Modeling and 3D Printing of Koch Fractal Contact and Interlocking, University of New Hampshire, 2017.

[22] Li, Y., C. Ortiz, M.C. Boyce, A generalized mechanical model for suture interfaces of arbitrary geometry, J. Mech. Phys. Solids. 61 (2013) 1144–1167. https://doi.org/10.1016/j.jmps.2012.10.004.

[23] Wang, W., Y. Sun, Y. Lu, J. Wang, Y. Cao, C. Zhang, Tensile behavior of bio-inspired hierarchical suture joint with uniform fractal interlocking design, J. Mech. Behav. Biomed. Mater. 113 (2021) 104137. https://doi.org/10.1016/j.jmbbm.2020.104137.

[24] Peterman, D.J., K.A. Ritterbush, C.N. Ciampaglio, E.H. Johnson, S. Inoue, T. Mikami, T.J. Linn, Buoyancy control in ammonoid cephalopods refined by complex internal shell architecture, Sci. Rep. (2021) 1–12. https://doi.org/10.1038/s41598-021-87379-5.

[25] Wang, G., Y. Gu, L. Zhao, J. Xuan, G. Zeng, Z. Tang, Y. Sun, Experimental and numerical investigation of fractal-tree-like heat exchanger manufactured by 3D printing, Chem. Eng. Sci. 195 (2019) 250–261. https://doi.org/10.1016/j.ces.2018.07.021.

[26] Paniagua-Guerra, L.E., S. Sehgal, C.U. Gonzalez-Valle, B. Ramos-Alvarado, Fractal channel manifolds for microjet liquid-cooled heat sinks, Int. J. Heat Mass Transf. 138 (2019) 257–266. https://doi.org/10.1016/j.ijheatmasstransfer.2019.04.039.

[27] Mazur, M., T. Bhatelia, B. Kuan, J. Patel, P.A. Webley, M. Brandt, V. Pareek, R. Utikar, Additively manufactured, highly-uniform flow distributor for process intensification, Chem. Eng. Process. - Process Intensif. 143 (2019) 107595. https://doi.org/10.1016/j.cep.2019.107595.

[28] See, Y.S., K.C. Leong, Fabrication of minichannel fractal flow channels by selective laser melting for two-phase flow cooling applications, in: Proc. Int. Conf. Prog. Addit. Manuf., 2018: pp. 667–672. https://doi.org/10.25341/D4JP45.

[29] Ha, N.S., T.M. Pham, W. Chen, H. Hao, G. Lu, Crashworthiness analysis of bio-inspired fractal tree-like multi-cell circular tubes under axial crushing, Thin-Walled Struct. 169 (2021) 108315. https://doi.org/10.1016/j.tws.2021.108315.

[30] Wu, J., Y. Zhang, F. Zhang, Y. Hou, X. Yan, A bionic tree-liked fractal structure as energy absorber under axial loading, Eng. Struct. 245 (2021) 112914. https://doi.org/10.1016/j.engstruct.2021.112914.

[31] Zhang, Y., M. Lu, C.H. Wang, G. Sun, G. Li, Out-of-plane crashworthiness of bio-inspired self-similar regular hierarchical honeycombs, Compos. Struct. 144 (2016) 1–13. https://doi.org/10.1016/j.compstruct.2016.02.014.

[32] Zhang, Y., J. Wang, C. Wang, Y. Zeng, T. Chen, Crashworthiness of bionic fractal hierarchical structures, Mater. Des. 158 (2018) 147–159. https://doi.org/10.1016/j.matdes.2018.08.028.

[33] Li, Z., L. Shen, K. Wei, Z. Wang, Compressive behaviors of fractal-like honeycombs with different array configurations under low velocity impact loading, Thin-Walled Struct. 163 (2021). https://doi.org/10.1016/j.tws.2021.107759.

[34] Liu, H., E.T. Zhang, B.F. Ng, In-plane dynamic crushing of a novel honeycomb with functionally graded fractal self-similarity, Compos. Struct. 270 (2021) 114106. https://doi.org/10.1016/j.compstruct.2021.114106.

[35] Wang, J., Y. Zhang, N. He, C.H. Wang, Crashworthiness behavior of Koch fractal structures, Mater. Des. 144 (2018) 229–244. https://doi.org/10.1016/j.matdes.2018.02.035.

[36] Dadrasi, A., M. Beynaghi, S. Fooladpanjeh, Crashworthiness of Thin-Walled Square Steel Columns Reinforced Based on Fractal Geometries, Trans. Indian Inst. Met. 72 (2019) 215–225. https://doi.org/10.1007/s12666-018-1475-9.

[37] Zhang, Y., N. He, X. Song, T. Chen, H. Chen, On impacting mechanical behaviors of side fractal structures, Thin-Walled Struct. 146 (2020) 106490. https://doi.org/10.1016/j.tws.2019.106490.

[38] He, Q., Y. Wang, H. Gu, J. Feng, H. Zhou, The dynamic behavior of fractal-like tubes with Sierpinski hierarchy under axial loading, Eng. Comput. (2021). https://doi.org/10.1007/s00366-020-01275-6.

[39] Calignano, F., D. Manfredi, E.P. Ambrosio, S. Biamino, M. Lombardi, E. Atzeni, A. Salmi, P. Minetola, L. Iuliano, P. Fino, Overview on additive manufacturing technologies, Proc. IEEE. 105 (2017) 593–612. https://doi.org/10.1109/JPROC.2016.2625098.

[40] Dudek, K.K., J.A.I. Martínez, G. Ulliac, M. Kadic, Micro-Scale Auxetic Hierarchical Mechanical Metamaterials for Shape Morphing, Adv. Mater. 34 (2022). https://doi.org/10.1002/adma.202110115.

[41] Warner, J., P. Soman, W. Zhu, M. Tom, S. Chen, Design and 3D Printing of Hydrogel Scaffolds with Fractal Geometries, ACS Biomater. Sci. Eng. 2 (2016) 1763–1770. https://doi.org/10.1021/acsbiomaterials.6b00140.

[42] Jilani, S.F., A.K. Aziz, Q.H. Abbasi, A. Alomainy, Ka-band Flexible Koch Fractal Antenna with Defected Ground Structure for 5G Wearable and Conformal Applications, IEEE Int. Symp. Pers. Indoor Mob. Radio Commun. PIMRC. 2018-Septe (2018) 361–364. https://doi.org/10.1109/PIMRC.2018.8580692.

[43] Ramasamy, M., V.K. Varadan, 3D printing of wearable fractal-based sensor systems for neurocardiology and healthcare, in: Nanosensors, Biosensors, Info-Tech Sensors 3D Syst. 2017, 2017: p. 1016709. https://doi.org/10.1117/12.2261386.

[44] James, S., R. Contractor, Study on Nature-inspired Fractal Design-based Flexible Counter Electrodes for Dye-Sensitized Solar Cells Fabricated using Additive Manufacturing, Sci. Rep. 8 (2018) 1–12. https://doi.org/10.1038/s41598-018-35388-2.

[45] Ajdari, A., B.H. Jahromi, J. Papadopoulos, H. Nayeb-Hashemi, A. Vaziri, Hierarchical honeycombs with tailorable properties, Int. J. Solids Struct. 49 (2012) 1413–1419. https://doi.org/10.1016/j.ijsolstr.2012.02.029.

[46] Monnerot-Dumaine, A., Greek cross 3D, (2006). https://commons.wikimedia.org/wiki/File:Greek_cross_3D.png (accessed February 11, 2022).

[47] Dickau, R., Greek Cross Fractal, (2008). https://www.robertdickau.com/greekcross.html (accessed February 10, 2022).

[48] Dickau, R., Greek cross 3D 1 through 4, (2008). https://commons.wikimedia.org/wiki/File:Greek_cross_3D_1_through_4.png (accessed February 11, 2022).

[49] Lu, H., W. Wu, J. Huang, X. Zhang, N. Yuan, Compact dual-mode microstrip bandpass filter based on greek-cross fractal resonator, Radioengineering. 26 (2017) 275–284.

[50] Tsarev, V.A., A.Y. Miroshnichenko, N.A. Akafyeva, Compact Double-Gap Resonator of Low-Voltage Multi-Beam Klystron with a Strip Resonance Fractal Structure of the Greek Cross Type, in: 2019 Syst. Signal Synchronization, Gener. Process. Telecommun., IEEE, 2019: pp. 1–4.

[51] Ye, L., Y. Chen, J. Zhou, H. Feng, Y. Zhang, Q.H. Liu, High-performance spoof surface plasmon polariton waveguides and splitters based on Greek-cross fractal units, J. Phys. D. Appl. Phys. 53 (2020) 235502.

[52] Jafferson, J.M., S. Pattanashetti, Use of 3D printing in production of personal protective equipment (PPE) - A review, Mater. Today Proc. 46 (2021) 1247–1260. https://doi.org/10.1016/j.matpr.2021.02.072.

[53] National Football League, NFL Helmet Challenge, (2019). https://www.nfl.com/playerhealthandsafety/equipment-and-innovation/innovation-challenges/nfl-helmet-challenge (accessed January 1, 2022).

[54] Kollide, (2021). https://www.kollide.ca/ (accessed January 1, 2022).

[55] Boutin, G., Shock-absorbing assembly and body protection device including same, U.S. Patent Application No.17/257,567, 2021.

[56] HEXR, No Title, (2021). https://hexr.com/ (accessed January 1, 2022).

[57] Khosroshahi, S.F., S.A. Tsampas, U. Galvanetto, Feasibility study on the use of a hierarchical lattice architecture for helmet liners, Mater. Today Commun. 14 (2018) 312–323. https://doi.org/10.1016/j.mtcomm.2018.02.002.

[58] Gao, W., X. He, J. Wang, Y.T. Feng, C. Wang, Numerical investigation of oblique impact behavior of a helmeted headform on a windshield considering failure, Thin-Walled Struct. 171 (2022) 108722. https://doi.org/10.1016/j.tws.2021.108722.

[59] 3D Printing Industry, Army's combat helmet, (n.d.). https://3dprintingindustry.com/news/general-lattice-secures-us-army-contract-to-improve-combat-helmets-with-3d-printing-196586/.

[60] Rice University, Rice tapped to develop 3D-printed 'smart helmets' for the military, (n.d.). https://news.rice.edu/news/2021/rice-tapped-develop-3d-printed-smart-helmets-military.

[61] Mehta, P.S., J. Solis Ocampo, A. Tovar, P. Chaudhari, Bio-Inspired Design of Lightweight and Protective Structures, SAE Tech. Pap. (2016). https://doi.org/10.4271/2016-01-0396.

[62] Najmon, J.C., J. Dehart, Z. Wood, A. Tovar, Cellular Helmet Liner Design through Bio-inspired Structures and Topology Optimization of Compliant Mechanism Lattices, SAE Int. J. Transp. Saf. 6 (2018) 217–235. https://doi.org/10.4271/2018-01-1057.

[63] Santos, F.A., H. Rebelo, M. Coutinho, L.S. Sutherland, C. Cismasiu, I. Farina, F. Fraternali, Low velocity impact response of 3D printed structures formed by cellular metamaterials and stiffening plates: PLA vs. PETg, Compos. Struct. 256 (2021) 113128. https://doi.org/10.1016/j.compstruct.2020.113128.

[64] Khosroshahi, S.F., H. Duckworth, U. Galvanetto, M. Ghajari, The effects of topology and relative density of lattice liners on traumatic brain injury mitigation, J. Biomech. 97 (2019) 109376. https://doi.org/10.1016/j.jbiomech.2019.109376.

[65] EOS GmbH - Electro Optical Systems, Material data sheet PA 2200, 2017. https://www.eos.info/en/additive-manufacturing/3d-printing-plastic/sls-polymer-materials/polyamide-pa-12-alumide.

[66] ISO, U.E., British Standards Institution, BS EN ISO 527-2:2012. Plastics-Determination of tensile properties-Part 2: Test conditions for moulding and extrusion plastics, 2012.

[67] Belingardi, G., R. Montanini, M. Avalle, Characterization of polymeric structural foams under compressive impact loading by means of energy-absorption diagram, Int. J. Impact Eng. 25 (2001) 455–472.

[68] Tancogne-Dejean, T., A.B. Spierings, D. Mohr, Additively-manufactured metallic micro-lattice materials for high specific energy absorption under static

and dynamic loading, Acta Mater. 116 (2016) 14–28. https://doi.org/10.1016/j.actamat.2016.05.054.

[69] Hodge, P.G., H.G. Hopkins, E.H. Lee, The theory of piecewise linear isotropic plasticity, in: Deform. Flow Solids/Verformung Und Fliessen Des Festkörpers, Springer, 1956: pp. 147–170. https://doi.org/10.1007/978-3-642-48236-6_14.

[70] Öztürk, İ., N. Kaya, F. Öztürk, Effects of material failure criteria on design of vehicle parts under impact loading, Int. J. Crashworthiness. 27 (2022) 80–91. https://doi.org/10.1080/13588265.2020.1774480.

[71] Nations, U., Uniform provisions concerning the approval of protective helmets and of their visors for drivers and passengers of motorcycles and mopeds, (2002) 1–194. http://www.unece.org/fileadmin/DAM/trans/main/wp29/wp29regs/505ep29.pdf.

[72] Calignano, F., F. Giuffrida, M. Galati, Effect of the build orientation on the mechanical performance of polymeric parts produced by multi jet fusion and selective laser sintering, J. Manuf. Process. 65 (2021) 271–282. https://doi.org/10.1016/j.jmapro.2021.03.018.

[73] de Sousa, R.A., R. Coelho, F. Teixeira-Dias, D. Gonçalves, Assessing the effectiveness of a natural cellular material used as safety padding material in motorcycle helmets, Simulation. 88 (2012) 580–591. https://doi.org/10.1177/0037549711414735.